Representations of the amacrine cell population underlying retinal motion anticipation

Michael D. Menz, Dongsoo Lee and Stephen A. Baccus
Department of Neurobiology, Stanford University School of Medicine, Stanford University

Corresponding author: Stephen Baccus, 259 Campus Drive, Fairchild Building, Stanford, CA
baccus@stanford.edu, 650-736-1512

Acknowledgements: This work was supported by grants from the Pew Charitable Trusts, McKnight Endowment Fund for Neuroscience, the Weston Havens Foundation, the Alfred P. Sloan Foundation and the E. Matilda Ziegler Foundation (S.A.B.). We thank Mihai Manu and David Kastner for intracellular recording of amacrine responses.

Abstract

Retinal amacrine cells are a diverse population of inhibitory interneurons, posing a challenge to understand the specific roles of those interneurons in computations of the similarly diverse ganglion cell population. Here we record from both populations simultaneously in the salamander retina to study the predictive computation of motion anticipation, which is thought to compensate for processing delays when encoding moving objects. We recorded the membrane potential of the amacrine cell population optically while recording electrically from ganglion cells with a multielectrode array. By correlating thousands of amacrine and ganglion cell pairs, we modeled the contribution of the traveling wave of activity for different amacrine cell populations to the encoding of a moving bar. We find that the population responses of slow transient amacrine cells can quantitatively account for ganglion cell motion anticipation, supporting a role for this specific amacrine cell class in the predictive encoding of moving stimuli.

Introduction

Neural circuits use interneurons to transform an input neuron representation into a neural output. Understanding this process is complicated by the fact that all three neural populations carry distinct signals. Even with the advent of new recording technologies, accessing all three populations is beyond reach in most cases. In the retina, the diversity of neural subtypes poses a significant problem towards understanding circuit function. In particular, inhibitory interneurons are extremely diverse, both in the retina (Masland, 2001) and higher brain (Monyer and Markram, 2004), but their specific functions are largely unknown. There are approximately one dozen types of bipolar cells, more than 30 amacrine cells, and more than one dozen ganglion cells. A critical barrier is the lack of the ability to observe simultaneously at multiple levels in the circuit. Furthermore, the diversity of both interneurons and retinal ganglion cells requires the observation of neural populations.

Voltage sensitive fluorescent dyes have been used to measure the membrane potential both of subcellular structures such as dendrites and axons, and to record cell populations in neural networks (Homma et al., 2009). Second harmonic generation (SHG) imaging has allowed the recording of membrane potential from single cells (Dombeck et al., 2004), as well as many neurons in a brain slice (Sacconi et al., 2008). Unlike two-photon fluorescence, where two coincident photons are absorbed and then a single photon is emitted after a shift in wavelength, SHG is an energy conserving process, converting two photons into a single photon at exactly

half the wavelength.

We focus on the signals carried in the amacrine cell population in relation the problem of how moving objects are represented in the ganglion cell population. Retinal responses to moving objects have multiple nonlinear properties, including the anticipation of moving objects (Berry et al., 1999; Johnston and Lagnado, 2015), object motion sensitivity (Olveczky et al., 2003) and responses to motion reversal (Schwartz et al., 2007) In the case of motion anticipation for a smoothly moving object, inhibition has been implicated, but specific inhibitory classes as well as a computational model of those effects are unknown.

Here we simultaneously present a visual stimulus to the intact retina, while recording optically from a population of interneurons and simultaneously recording from a population of retinal ganglion cells with a multielectrode array. This approach allows optical measurements of the membrane potential of dozens of interneurons using a two photon scanning laser microscope (TPLSM) and electrical recording from dozens of ganglion cells. From this data, we modeled the motion response in ganglion cells and in different classes of amacrine cells. Based on previous experiments injecting current into amacrine cells, we compute the expected spatiotemporal representation of the transmission from different populations of amacrine cells to individual ganglion cells.

.

Results

SHG optical responses are similar to intracellular recordings

We performed simultaneous SHG imaging and multielectrode recording using a custom two-photon microscope in the inverted configuration (Fig. 1, see Methods). The SHG signal is produced from polar molecules arranged in an anisotropic structure. Styryl dyes such as FM 4-64 arranged in a membrane produce a SHG signal that is sensitive to membrane potential. As the voltage-dependent SHG signal is primarily transmitted through the tissue – not emitted in all directions as in fluorescence imaging – the transparent retina is well suited to this technique.

Because the SHG signal is highly dependent on the membrane voltage, intracellular membranes contribute virtually no background signal, unlike fluorescent voltage sensitive dyes (Bianchini and Diaspro, 2008). In addition, a primary dye used for SHG imaging, FM 4-64, is well tolerated by neural tissue for prolonged periods of time (> 1 hour), unlike many fast voltage sensitive dyes that have a significant pharmacological effect on neural responses (Homma et al., 2009). FM 4-64 is most often used as a fluorescent dye simply to label membranes in studies of synaptic vesicle recycling, and thus this dye is well tolerated by neurons and synapses (Fernández-Alfonso and Ryan, 2004).

We imaged in the amacrine cell layer, which is the inner nuclear layer just proximal to the inner plexiform layer (Pang et al., 2002; 2004). In response to a uniform field flash or moving bar presented at 1 Hz, amacrine cells showed either Transient Off, Transient On, On-Off, Sustained Off, and Sustained On responses (Fig. 2a). which appeared. These responses appeared qualitatively similar to intracellular electrical recordings performed in separate retinas.

Visual responses to a moving bar in amacrine and ganglion cell populations

To measure simultaneous responses of amacrine and ganglion cells, we presented a smoothly moving black bar (132 μm wide, 1.26 mm/s) (Berry et al., 1999) against a red background whose trajectory repeated every one second. In four retinas, we recorded 122 ganglion cells,

365 amacrine cells and 4812 amacrine-ganglion simultaneously recorded cell pairs. The bar stimulated amacrine and ganglion populations simultaneously (Fig 35a), with cells at different spatial locations responding at different times (Fig. 3b,c ,4a,b). Off-type ganglion cells responded to the moving bar with short bursts of spikes occurring at different times and durations (Fig 3c). Off-type ganglion cells were classified into “slow”, “medium”, and “fast” based on their temporal filters measured from a checkerboard white noise stimulus (Fig 3d). Amacrine cells were classified into three types depending on their response to the dark moving bar: depolarized (Off type, 153 cells), hyperpolarization followed by depolarization (biphasic type, 122 cells) or hyperpolarized (On type, 90 cells), with latencies and durations that differed between cells (Fig. 3, e-g). Intracellular responses to the moving bar did not necessarily correspond in a one to one manner to the flash response, as cells with On-Off responses to a flash could have different types of responses to a moving bar (Fig 2b).

Correlations between amacrine and ganglion cell populations

For a moving bar stimulus, we computed the correlation between amacrine and ganglion cells as the average amacrine cell response triggered on the spike of the ganglion cell. Figure 4 shows examples of amacrine cell responses relative to ganglion cell spiking for On, Biphasic and Off amacrine cells. By combining many cell pairs at different locations, we constructed a spatiotemporal representation of the average Off amacrine cell response at different stimulus distances and times relative to a Fast-Off-type ganglion cell spike (Fig. 4b). This map showed a wave of amacrine cell activity sweeping across the retina at the time a ganglion cell fired a spike. The velocity of the wave was computed by a linear regression to the peak of the amacrine response as a function of position, where computed velocity was 1.27 mm/s, compared to the actual bar velocity of 1.26 mm/s. A space-time map was constructed for each combination of ganglion cell type (fast, medium, slow) and each amacrine cell type (Off-Top, Biphasic-Middle, On-Bottom). Fig. 4c shows the temporal distribution of amacrine responses for nearby (within 20 μm) amacrine-ganglion cell pairs for all nine combinations of cell pair types. In general, the peak amacrine depolarization occurred soon after the ganglion cell spiked for Off and Biphasic type amacrine cells (Fig. 4c, Top and Middle), with variations in timing that are dependent on ganglion cell type. For On amacrine cells, which are expected to be excitatory to Off-type ganglion cells, peak hyperpolarization occurs near the time of the ganglion cell spike, with membrane potential reaching a minimum either just after before after the ganglion cell spike depending on the ganglion cell type. Examining the spatial distribution of the amacrine cell response at the time ganglion cell’s spike, we found that the most depolarized amacrine cells trail the moving bar. Different amacrine cell classes showed different population spatiotemporal activity relative to the time of a ganglion cell spike.

We then used the spatiotemporal map of amacrine activity to predict the effect Off amacrine cells would have on Fast-Off ganglion cells (Fig 4d). To do so, we needed to estimate the timing and spatial extent and temporal delay of their transmission. For sustained Off-type amacrine cells, we used previous measurements of their temporal transmission filter computed from intracellular studies, which we modeled as an exponential spatial decay of 83 μm, and a monophasic negative temporal filter with a time to peak of 25 ms (Manu and Baccus, 2011). After transforming the amacrine population response with this transmission filter, the result is a spatiotemporal map of the estimated effect from amacrine cells at each spatial position and time. Integrating across space yielded an estimate of the total effect of the amacrine population as a function of time relative to a ganglion cell’s spike (Fig 4e Left). From this estimated population effect, maximum disinhibition occurs several hundred millisecond before spiking, inhibition during spiking, and maximum inhibition at about 150 ms after spiking. Then at the time of a ganglion cell spike, we examined the spatial distribution of amacrine effects (Fig 4e, Right). The largest inhibition is coming from nearby cells in the direction the bar has just passed (left of zero), which is a consequence of the spatial weighting. The distribution around zero is not

symmetrical, with more inhibition coming from the amacrine cells that preceded the ganglion cells.

Specific amacrine types create different inputs during motion anticipation

For an object moving over a range of speeds, ganglion cell responses compensate for neural processing delays by anticipating the object's motion, creating a traveling wave of activity that matches the leading edge of the object (Berry et al., 1999; Johnston and Lagnado, 2015). We characterized the type and extent of motion anticipation by comparing ganglion cell responses to those predicted by a simple linear-nonlinear (LN) model consisting of a spatiotemporal linear filter followed by a static (time independent) nonlinear function. We fit LN models to a white noise checkerboard stimulus, and then used the model to predict the response to a moving bar. Many cells showed motion anticipation in that the response was earlier in time on average than the LN model prediction. For these cells, in most cases the firing rate response and LN prediction began at the same time, and the cell's response was truncated earlier than the LN model's prediction, conforming to previous models of motion anticipation (Berry et al., 1999; Johnston and Lagnado, 2015). We termed this type of response 'motion adaptation'. However, in 17 % of cells, the cell's response began earlier than the LN model's prediction, a type of motion anticipation that we termed 'motion prediction' (Fig. 5b). These cells exhibited greater motion anticipation than motion adapting cells, and motion predicting cells responded earlier to the moving bar than motion adapting cells (Supp. Fig. 3). Motion adapting and motion predicting cells did not map specifically onto ganglion cell types, as for either of the two motion types the percentage fast-Off, slow-Off and medium-Off ganglion cell classes were not substantially different (Chi squared test $p > 0.3$, Supp. Fig. 3). Previous models of motion anticipation consisted of a truncation of the linear response through feedback or feedforward inhibition (Berry et al., 1999; Johnston and Lagnado, 2015). Motion predicting cells are inconsistent with this model, and thus represented a second type of motion anticipation.

To test the potential role of different amacrine cell populations in motion anticipation for these two classes of ganglion cells, we used the measured amacrine cell population responses to account for the difference in the ganglion cell response from an LN model. We clustered the amacrine responses into four types, based on their responses to moving bars, as shown in Fig 3e (Off, Fast Biphasic, Slow Biphasic and On). These responses were then delayed in time by 25 ms and filtered spatially as in Fig. 5 to represent the effect of each amacrine cell on each ganglion cell. Two different types of models were then considered. In the first model, the amacrine responses acted to control the gain of ganglion cells via a divisive mechanism. This Divisive Linear Nonlinear (DLN) was a modification the LN model that took the measured amacrine responses and controlled the gain of the output of the linear filter via a divisive effect. This model had only four additional parameters from the LN model, which represented the weighting of each of the four amacrine cell classes of the optically measured responses. The second model type we named the Subtractive Linear Nonlinear (SLN) model, which similarly took the measured amacrine cell responses and subtracted them from the linear filter output of the LN model with one weight parameter for each of the four amacrine classes. In both cases, the nonlinearity was the same as the LN model.

In both of these models, note that we expect that amacrine cells also contribute to the linear filter, so the use of the amacrine cell responses in the SLN and DLN models represented strictly the nonlinearity effects of these amacrine cells. Any linear effects were contained in the initial linear filter of the LN model, but were not explicitly separated out for any model.

We found that either the DLN or SLN models could fit cells whose response onset matched the LN model, but that only the SLN model could fit cells that responded earlier than the LN model. This is expected because a divisive gain control could not advance the onset of the response to a time earlier than the onset of the linear filter output to match the earlier

response of the data. We thus used fits to the SLN and DLN model to classify whether a cell exhibited motion adaptation or motion prediction, in that cells that were more accurately fit by the SLN model than the DLN model were classified as exhibiting motion prediction.

We then examined the parameters of the model to assess whether certain amacrine cell types contributed more to the prediction of the ganglion cell response. We found that the weights in the model were different for different amacrine types, but were similar for motion adapting cells and for motion predicting cells for the subtractive and divisive models (Fig. 5e) Slow biphasic and Off amacrine cells having the greatest contribution in the model, whereas On type amacrine cells contributed little for either model. Slow and fast biphasic amacrine cells had a greater contribution to motion predicting cells than for motion adapting cells. In addition, across the population, the weights of slow biphasic amacrine cells were strongly correlated with the amount of motion anticipation across cells, with cells that showed greater motion anticipation having a greater weight in the model from slow biphasic cells (r = 0.7, Fig. S3c).

Discussion

In this study we have controlled visual input to a population of photoreceptors, while simultaneously measuring optically from a population of interneurons and recording electrically from a population of retinal ganglion cells, allowing access to all layers of cell bodies in the retina. In doing so, we have examined populations of amacrine cells that are likely to contribute to motion anticipation. Previously it was proposed that motion anticipation results from general inhibitory properties of the retina (Johnston and Lagnado, 2015). In contrast, our results point to distinct populations of amacrine cells as contributing to motion anticipation. Specifically, On-Off amacrine cells with slow biphasic responses to a moving bar are the most likely cell classes to contribute to motion anticipation.

As shown in Fig 5 there is a wide range in the timing of inhibition coming from individual amacrine cells. However, if we average across all individual amacrines of one type (e.g., Off vs Biphasic), then it is notable that the inhibition from these different cell types arrives at approximately the same time for the medium and fast ganglion cells (Fig 4c, Left Top and Left Middle, red and black traces). The peak of inhibition occurs soon after spiking which could truncate the ganglion response in time, moving the peak earlier consistent with motion anticipation.

It has been previously suggested that a gain control mechanism could generate motion anticipation (Berry et al., 1999). We confirm that a gain control mechanism (our divisive model) can account for the motion anticipation for most ganglion cells. However, it is clear that motion predicting cells have a response that could not be generated simply by divisive gain control applied to the linear response (Fig 5). A subtractive effect of amacrine inhibition is intrinsically more versatile because membrane voltage can be depolarized or hyperpolarized at whatever time it is needed. Comparing motion predicting to motion adaptive cells in the subtractive model, the biggest difference between the two cell classes is the value of the weights from slow Biphasic amacrines (Fig 5e). Furthermore, the slow Biphasic amacrines have the strongest correlation with motion anticipation (Fig. S3c). These results suggests that slow Biphasic amacrines play a more important role in motion anticipation compared to the other amacrine cell types, in particular as to cells that exhibit the greatest amount of motion anticipation, the motion predicting cells.

It has also been proposed that amacrine cell inhibition could be the mechanism responsible for gain control (Johnston and Lagnado, 2015) and we confirm that as well. However, this previous

work suggested a very simple model that consists of an excess of inhibitory inputs over excitatory inputs that are both randomly distributed. Our study is more consistent with a circuit that has specific connections between specific cell types as is known for other motion-related phenomena such as direction selectivity and objection motion sensitivity (Euler et al., 2002) (Baccus et al., 2008). We find a significantly more important role for the slow Biphasic amacrines cells for motion predicting cells, while Off and slow Biphasic are equally important for motion adapting cells.

The models that include measured amacrine cell responses account for the deviation in ganglion cell response from the expected output of the ganglion cell linear receptive field, a deviation that represents the motion anticipation phenomenon (Berry et al., 1999; Johnston and Lagnado, 2015). But it may well be that the amacrine cells also contribute to that linear prediction, and that amacrine cell linear contribution is not explicitly shown in our models. A more mechanistic model of motion anticipation would eliminate this distinction between the linear receptive field and nonlinear contribution of amacrine cells, and just define one contribution of amacrine cells that accounts for both. This model would require optical recording of the amacrine population under a more rich stimulus set such as white noise to map receptive fields, which we have not done here. To complete such models, direct perturbation of individual amacrine cell types (Manu & Baccus, 2011; Kastner et al., 2019) will be needed to define their precise spatiotemporal contributions to motion anticipation. Our population measurements from interneurons and retinal outputs will direct such future studies, and point out the benefit of simultaneous recording of interneurons and circuit output to understand how diverse types of interneurons shape the diverse types of ganglion cells in the retina.

References

Baccus SA, Meister M (2002) Fast and slow contrast adaptation in retinal circuitry. Neuron 36:909–919.

Baccus SA, Olveczky BP, Manu M, Meister M (2008) A retinal circuit that computes object motion. J Neurosci 28:6807–6817.

Berry MJ, Brivanlou IH, Jordan TA, Meister M (1999) Anticipation of moving stimuli by the retina. Nature 398:334–338.

Bianchini P, Diaspro A (2008) Three-dimensional (3D) backward and forward second harmonic generation (SHG) microscopy of biological tissues. J Biophotonics 1:443–450.

Chichilnisky EJ (2001) A simple white noise analysis of neuronal light responses. Network 12:199–213.

Chu SW, Liu TM, Sun CK (2003) Real-time second-harmonic-generation microscopy based on a 2-GHz repetition rate Ti : sapphire laser. Opt Express 11:933–938.

de Vries SEJ, Baccus SA, Meister M (2011) The projective field of a retinal amacrine cell. J Neurosci 31:8595–8604.

Denk W, Detwiler PB (1999) Optical recording of light-evoked calcium signals in the functionally intact retina. Proc Natl Acad Sci USA 96:7035–7040.

Dombeck DA, Blanchard-Desce M, Webb WW (2004) Optical recording of action potentials with second-harmonic generation microscopy. J Neurosci 24:999–1003.

Dombeck DA, Sacconi L, Blanchard-Desce M, Webb WW (2005) Optical recording of fast neuronal membrane potential transients in acute mammalian brain slices by second-harmonic generation microscopy. J Neurophysiol 94:3628–3636.

Euler T, Detwiler PB, Denk W (2002) Directionally selective calcium signals in dendrites of starburst amacrine cells. Nature 418:845–852.

Fernández-Alfonso T, Ryan TA (2004) The kinetics of synaptic vesicle pool depletion at CNS

synaptic terminals. Neuron 41:943–953.
Homma R, Baker BJ, Jin L, Garaschuk O, Konnerth A, Cohen LB, Zecevic D (2009) Wide-field and two-photon imaging of brain activity with voltage- and calcium-sensitive dyes. Philos Trans R Soc Lond, B, Biol Sci 364:2453–2467.
Jiang J, Eisenthal KB, Yuste R (2007) Second harmonic generation in neurons: electro-optic mechanism of membrane potential sensitivity. Biophys J 93:L26–L28.
Johnston J, Lagnado L (2015) General features of the retinal connectome determine the computation of motion anticipation. Elife 4.
Kastner DB, Baccus SA (2013) Spatial Segregation of Adaptation and Predictive Sensitization in Retinal Ganglion Cells. Neuron 79:541–554.
Kastner DB, Ozuysal Y, Panagiotakos G (2019) Adaptation of inhibition mediates retinal sensitization. Curr Biol 29(16):2640-2651.
Manu M, Baccus SA (2011) Disinhibitory gating of retinal output by transmission from an amacrine cell. Proc Natl Acad Sci USA 108:18447–18452.
Masland R (2001) The fundamental plan of the retina. Nat Neurosci 4:877–886.
Millard AC, Jin L, Wei M-D, Wuskell JP, Lewis A, Loew LM (2004) Sensitivity of second harmonic generation from styryl dyes to transmembrane potential. Biophys J 86:1169–1176.
Millard AC, Jin L, Wuskell JP, Boudreau DM, Lewis A, Loew LM (2005) Wavelength- and time-dependence of potentiometric non-linear optical signals from styryl dyes. J Membr Biol 208:103–111.
Monyer H, Markram H (2004) Interneuron Diversity series: Molecular and genetic tools to study GABAergic interneuron diversity and function. Trends Neurosci 27:90–97.
Moreaux L, Sandre O, Blanchard-Desce M, Mertz J (2000) Membrane imaging by simultaneous second-harmonic generation and two-photon microscopy. Opt Lett 25:320–322.
Nemet BA, Nikolenko V, Yuste R (2004) Second harmonic imaging of membrane potential of neurons with retinal. J Biomed Opt 9:873–881.
Nuriya M, Jiang J, Nemet B, Eisenthal KB, Yuste R (2006) Imaging membrane potential in dendritic spines. Proc Natl Acad Sci USA 103:786–790.
Olveczky BP, Baccus SA, Meister M (2003) Segregation of object and background motion in the retina. Nature 423:401–408.
Pang J-J, Gao F, Wu SM (2002) Segregation and integration of visual channels: layer-by-layer computation of ON-OFF signals by amacrine cell dendrites. J Neurosci 22:4693–4701.
Pang J-J, Gao F, Wu SM (2004) Stratum-by-stratum projection of light response attributes by retinal bipolar cells of Ambystoma. J Physiol (Lond) 558:249–262.
Pologruto TA, Sabatini BL, Svoboda K (2003) ScanImage: flexible software for operating laser scanning microscopes. Biomed Eng Online 2:13.
Reeve JE, Anderson HL, Clays K (2010) Dyes for biological second harmonic generation imaging. Phys Chem Chem Phys 12:13484–13498.
Sacconi L, Dombeck DA, Webb WW (2006) Overcoming photodamage in second-harmonic generation microscopy: real-time optical recording of neuronal action potentials. Proc Natl Acad Sci USA 103:3124–3129.
Sacconi L, Mapelli J, Gandolfi D, Lotti J, O'Connor RP, D'Angelo E, Pavone FS (2008) Optical recording of electrical activity in intact neuronal networks with random access second-harmonic generation microscopy. Opt Express 16:14910–14921.
Schwartz G, Taylor S, Fisher C, Harris R, Berry MJ (2007) Synchronized firing among retinal ganglion cells signals motion reversal. Neuron 55:958–969.
Teisseyre TZ, Millard AC, Yan P, Wuskell JP, Wei M-D, Lewis A, Loew LM (2007) Nonlinear optical potentiometric dyes optimized for imaging with 1064-nm light. J Biomed Opt 12:044001–.
Theer P, Denk W, Sheves M, Lewis A, Detwiler PB (2011) Second-harmonic generation imaging of membrane potential with retinal analogues. Biophys J 100:232–242.

Figure Legends

Figure 1. Second harmonic imaging of amacrine cells (a) Setup for simultaneous two-photon imaging and multielectrode recording of visual responses. Left. Schematic diagram showing light paths for SHG illumination, collection and visual stimulation. The laser is focused through an objective below the retina. The SHG signal is collected on the opposite side of the retina by an objective and reflected to a photomultiplier tube (PMT). The upper objective also focuses the visual stimulus onto the retina. Right. Expanded view of microscope objectives and the retina, which is placed ganglion side down on a multielectrode array. Drawing is not to scale. (b) Left. An SHG image in the inner nuclear layer just above the inner plexiform layer, 55 μ m above the array. Two recordings were made 90° apart in polarization angle and combined in two different color channels of the image, with 0° in green and 90° in red. Yellow pixels respond equally to both polarization angles. Right. Scatterplot of all pixel values from the SHG image for different polarization angles or from two separate images at the same polarization angle. (c) Cross-section (XZ) projection of retinal stack, array at the bottom. Left. Fluorescent image. PRL=photoreceptor layer, red line is outer plexiform layer, INL=inner nuclear layer, IPL=inner plexiform layer, GCL=ganglion cell layer. Right. Second Harmonic Signal (SHG) image (d) Left. Depth (Z) projection of fluorescent image from (c). Middle. Depth (Z) projection of SHG image from c(). Right. Normalized ratio of SHG to Fluoresence depth projections. Dotted lines indicate borders between layers, red dotted line indicates center of outer plexiform layer.

Figure 2. Cell types of SHG recordings. (a) Left. SHG responses (black) from different types of amacrine cells to a uniform field flash of light at 1 Hz, each trace a different cell, showing representative examples for the five major types. Responses are the average of 140 trials. Right. Example intracellular recordings (red) recorded separately from different cells and retinas to a uniform field flash of light at 0.5 Hz. (b) Moving bar responses from individual amacrine cell SHG recordings (black) compared to similar single cell intracellular recordings from different preparations (red) classified by their intracellular flash response. All responses are to black bars moving against a bright background.. SHG responses are classified as Off for the top two cells, Biphasic for the middle cell, and On for the bottom two cells.

Figure 3. Simultaneous recording of amacrine and ganglion cell populations to moving stimuli. (a) Left. Space-time plot of the trajectory of the bar shown at a spatial cross section indicated by the vertical grey line at right. Right. Spatial layout of visual stimulus, electrode arrays and imaged areas as projected onto the retina. A 132 μm black bar moved at a speed of 1.26 mm/s against a red background (pink area). The electrode array had two groups of 30 electrodes each covering an area of 150 μm x 120 μm and spaced 620 μm apart. Four locations were imaged sequentially in a single retina. Each location was laterally offset (88 μm from border of array to border of imaged area or 200 μm from center of array to center of imaged area) to an electrode group . The electrode array is indicated by the blue rectangle. The green rectangle indicates the area imaged using the two-photon microscope. (b) Left. Peristimulus time histograms (PSTHs) of 122 ganglion cell PSTHs ordered vertically by latency, pooled over four retinas. Each row is a different cell, and color indicates firing rate. (c) Example PSTHs from five ganglion cells. (d) Ganglion cells were clustered by k-means into fast, medium and slow types based on temporal filters measured using a white noise checkerboard stimulus. (e) SHG responses from 365 amacrine cells pooled over four retinas categorized into three classes, Off, Biphasic and On. Responses are ordered by latency. (f) Example SHG responses are shown for eight cells. (g) Biphasic amacrine cells are further subdivided into fast and slow by k-means clustering to be used in the model of Fig. 5.

Figure 4. Prediction of effects of the amacrine cell population on ganglion cell responses (a) Diagram depicting the distance between amacrine and ganglion cells measured along the direction of a moving bar. (b) Space-Time plot of the average population Off amacrine activity relative to the time of a spike of Fast Off ganglion cells (n=835 pairs), computed as the spike-triggered average of amacrine cell responses binned by amacrine-ganglion cell distance in the direction of the moving bar. Cellular location was taken as the amacrine soma location and the ganglion cell receptive field center. Negative values of stimulus distance indicate the bar encountered the amacrine cell before the ganglion. (c) Left. Temporal slices of amacrine-ganglion cell correlations for different amacrine and ganglion cell classes for nearby cell pairs (< 20 µm in the direction of motion). Top Left. Temporal slices from Space-Time plots taken with Off amacrine cells and Off ganglion cells (fast, 835 pairs, medium, 965 pairs, slow, 272 pairs). Middle Left. Temporal slices from Space-Time plots taken with Biphasic amacrine and Off ganglion cells (fast, 692 pairs, medium, 715 pairs, slow, 189 pairs). Bottom Left. Temporal slices from Space-Time plots taken with On amacrines and Off ganglion cells (fast, 472 pairs, medium, 484 pairs, slow, 169 pairs). Right. Spatial slices from Space-Time plots of different amacrine cell types averaged across all ganglion cells presented when the ganglion cell spikes. Top Right. Spatial slice of Space-Time plot for Off amacrines averaged across all ganglion cells (n=2090 total pairs). Middle Right. Spatial slice of Space-Time plot for Biphasic amacrines averaged across all ganglion cells (1596 total pairs). Bottom Right. Spatial slice of Space-Time plot for On amacrines averaged across all ganglion cells (1125 total pairs). (d) The spike-triggered average responses from panel (b) were filtered by an average amacrine cell transmission filter (25 ms delay) computed from previous intracellular studies (Manu and Baccus, 2011) and spatially weighted with a space constant of 83 microns (Manu and Baccus, 2011), then inverted in sign to predict the average effect the Off amacrine cell population on the average Fast Off ganglion cell, relative disinhibition in white, inhibition in black. (e) Left. Integration along the spatial axis from part (d) yields an estimate of the relative disinhibition and inhibition an average 'fast' off ganglion cell would receive from a spatially distributed population of Off amacrine cells. Right. Spatial distribution of inhibition from panel (d) taken within 25 ms of a ganglion cell spike.

Figure 5. Specific amacrine responses underlie motion anticipation. (a) Models of motion anticipation combining the linear receptive field with measured amacrine cell responses. The moving bar stimulus S(x,t) is convolved with the space-time receptive field RF(x,y,t) of the ganglion cell as measured with white noise. This linear prediction serves as the first stage of one of three models 1) A Linear-Nonlinear (LN) model that simply passes the linear prediction through a threshold. 2) The gain of the linear prediction is divisively controlled by a weighted linear combination of amacrine cell responses prior to the nonlinearity (Divisive LN or DLN model) 3). The linear prediction is summed with a weighted linear combination of amacrine cell responses prior to the nonlinearity (Subractive LN or SLN model). Four scalar weights on different amacrine cell classes are optimized to fit the model's output to the data (one for each of Off, slow Biphasic, fast Biphasic and On amacrine cell populations). (b) Left. An example ganglion cell with motion anticipation of 26 ms (difference in the temporal center of mass of firing rate, LN vs. Data) in which the divisive gain control (DLN) model can account for motion anticipation, termed a Motion Adapting cell. Middle. An example ganglion cell with motion anticipation of 60 ms in which the cell's response precedes the linear prediction, termed a Motion Predicting cell. Right. Scatterplot of the squared correlation coefficient (r^2) for the SLN model (subtractive) vs. data compared to the DLN model (divisive). Red line is the identity line. Cells that exhibited motion anticipation for which the SLN model substantially exceeded the DLN model were classified as Motion Predicting cells. (c). Average motion anticipation index for Motion Predicting (mean = 85 ms) and Motion Adapting cells (mean = 36 ms) ($p < 3.6e-10$, Wilcoxon-Mann-Whitney two-sample rank test). (d) Top Left. For a Motion Adapting cell, the

weighted amacrine cell input average over the total amacrine population for four different amacrine cell classes, using the optimal weighting for the DLN model (one scalar weight for each of four cell classes). Top Right. Nonlinearity of example DLN model. Bottom. For a Motion Predicting cell, the amacrine input and nonlinearity for an SLN model. (e) Average amacrine cell synaptic weights by model type (DLN or SLN) and ganglion cell type (Adapting or Predicting) and amacrine type (Off, fast Biphasic, slow Biphasic, and On). The DLN model did not effectively fit Motion Predicting ganglion cells.

Supplemental Figures Legends

Figure S1. Intracellular recording of a sustained Off amacrine cell with and without laser scanning. A binary random checkerboard stimulus was used to compute a linear-nonlinear model of the cell (a) Left. Spatial receptive field. Middle. Temporal filter. Right. Static non-linearity of LN model. (b) Left. Average response to 0.5 Hz uniform flash. Middle. Average response to laser scanning at 10Hz. Right. Right. Average response to laser scanning at 20Hz. (c) LN model measured with uniform gaussian white noise stimulus with 12% contrast without laser scanning (black) and with 10 Hz laser scanning (red). Left, temporal filter. Right. Non-linearity, which is linear in this case, showing that the visual response gain does not change when the laser is on.

Figure S2. Signal-to-Noise of SHG recordings. (a) ROI intensity from one amacrine cell binned relative to stimulus time (uniform field, one second on, one second off). Top. 25ms bins. Middle. 10ms bins. Bottom. 5 ms bins. (b) Same cell as in (a), binned at 25 ms, with the total 140 seconds of recording time subdivided into five equal parts showing how the average response changes during the recording. (c) Histogram of signal-to-noise ratio for 365 amacrine cells (average is 3.7). A value of 2.0 was the minimum to be included in the study.

Figure S3. (a) Left. Scatterplot of squared correlation coefficient (r^2) for the DLN model (divisive, average $r^2 = 0.66$) compared to the LN model (average $r^2 = 0.32$). Red line is the identity. Right Same for the SLN model (subtractive, average $r^2 = 0.72$) compared to the LN model. (b) Histogram of difference in r^2 for the SLN and DLN models (SNL - DLN). A k-means clustering with a value of 2 clusters (average Silhouette score = 0.89) divides the data into two classes, the Motion Adapting group (102 out of 122 cells) that are equally well fit by SLN and DLN models, and the Motion Predicting group where the SLN model exceeds the DLN model in accuracy (20 out of 122 cells). (c) Scatterplot comparing the motion anticipation index (temporal center of mass, LN model – data) and the weights on the slow biphasic type of amacrine cells for the SLN model (red = adapting cells, black = predicting cells, $r = 0.7$, $p[t2] < 3.9e-18$). (d) Fraction of ganglion cells of different types based on classification of temporal filter speed (fast, medium, slow) computed separately for Motion Adapting and Motion Predicting cells.

Methods

Multielectrode recording

Multielectrode array methods for extracellular recording and analysis were as described (Manu and Baccus, 2011). The salamander retina was isolated intact, and the photoreceptor side was adhered by surface tension to a dialysis membrane attached to a plastic holder. The retina holder was then placed on a motorized manipulator and lowered onto a 60-electrode array (ThinMEA, Multichannel Systems) ganglion cell side down. In this way, a large piece of retina, up to its entirety, was placed on the array with minimal disturbance to the neural circuitry. The multielectrode array was patterned on a coverslip (~180 μm thickness) allowing imaging from below through the array. The 10 μm diameter electrodes were separated by either 100 μm (low-density array) or 30 μm (high-density array). The array formed the bottom of a perfusion chamber, through which flows oxygenated Ringer solution buffered with bicarbonate. The full waveform of signals from the array of electrodes were digitized at 10 kHz and recorded on a computer.

Custom two-photon laser scanning microscope

A two-photon laser-scanning microscope was constructed in an inverted configuration to simultaneously perform multielectrode array recordings. A simplified diagram of essential elements is shown in (Fig. 1a). Excitation was provided by a mode-locked Ti:sapphire (Tsunami, Spectra-Physics) laser operated at 970 nm. For SHG imaging, three main optical pathways were used: (1) The laser beam entered the microscope from the bottom and was focused on the retina by a x40 1.2 NA (Zeiss) objective. (2) The SHG signal was collected from above the retina through a x40 0.8 NA (Leica) objective. This signal at half the excitation wavelength (485nm) was reflected (Z488RDC dichroic, Chroma) into a PMT (H7422-P, GaAsP from Hamamatsu) through a filter (FF01-488/20, Semrock) and a laser-blocking filter (FF01-680/SP, Semrock). (3) The visual stimulus delivered from a CRT video monitor was reflected to the microscope (FF735 dichroic, Semrock) and focused on the retina through the upper 0.8 NA x40 objective.

The multielectrode array and the retina were mounted on a fixed stage. To image different areas of the retina, the inverted microscope, including the x-y scanning galvanometer mirrors (VM-500, GSI Lumonics) were moved on an x-y stage. Each stage moved along the entering optical axis of the laser, thus not altering laser alignment. The software used to control the mirrors and save the images was Scanimage (Pologruto et al., 2003).

Imaging

In SHG imaging, the largest signal is scattered in the forward direction (Moreaux et al., 2000). Normally the collection objective would have a numerical aperture equal to or larger than the excitation objective to collect all the scattered light (Moreaux et al., 2000). Because of mechanical constraints, including the retina holder and micropipette, a long working distance necessitated a lower numerical aperture objective. Thus we underfilled the 1.2 NA laser excitation objective so that it effectively functioned as a 0.8 NA objective, allowing the 0.8 NA collection objective to capture all of the forward-scattered SHG signal. The average power at the sample was ~10 mW which is comparable to the laser power used (Denk and Detwiler, 1999) for calcium imaging in salamander retina (λ =930nm, 2-30mW).

The styryl dye FM 4-64 was bath applied by immersing the isolated retina in 82 μM (100 μg in 2ml) FM4-64 in oxygenated Ringer's for about 1 hr prior to its placement on the multi-electrode array. When the dye is applied extracellularly, a depolarization of the membrane reduces the measured SHG signal (Sacconi et al., 2006). SHG responses are displayed so that depolarization is shown in the upward direction. In these studies we did not directly measure

the relationship between SHG intensity change and voltage change for the dye FM4-64, although in previous studies this relationship ranges from 7.5 to 14 % / 100 mV (Dombeck et al., 2005; Nuriya et al., 2006; Sacconi et al., 2008). As the range of amacrine cell responses we measure range from 1 to 10%, this puts the response in the expected range (tens of mV) for amacrine cells. Note however, that because we measure SHG measurements for relative sensitivity to the stimulus and correlation with ganglion cells, we don't interpret the absolute amplitude of the voltage response.

The laser scanned an area of 164 x 73 μm (288 pixels x 128 pixels) bi-directionally in x (fast) and unidirectionally in y (slow) at a frame rate of 20 Hz (0.4 ms/line) about 55 μm above the multielectrode array in the amacrine cell layer, which is in the inner nuclear layer just proximal to the inner plexiform layer (Pang et al., 2002; 2004). The visual stimulus was uncorrelated with laser scanning so that each time the laser sampled a point in space it was in a different part of the stimulus cycle.

The SHG signal was strongly dependent on the polarization angle of the laser compared to the orientation of the dye molecules in the membrane (Jiang et al., 2007). Two laser polarization angles that were 90° apart produce an SHG signal from different parts of the soma (Fig 1b, left), showing that signals were SHG and not fluorescence (Fig 1b,right). For physiological recordings, only one laser polarization is used (0°, green areas in Fig 1b).

A second PMT located below the retina was used to capture fluorescent images for histological comparison with simultaneously measured SHG images. This was done when no visual stimulus was present, as the red emission fluorescence of FM 4-64 overlaps the red visual stimulus. A stack of images spanning 120 μm with 1 μm spacing was taken to compare SHG and fluorescence signals (Fig. 1c). Both fluorescence and SHG signals were brighter in the IPL, by virtue of high density of processes there. However the ratio of SHG to fluorescence differed across retinal layers, and in fact was lower in the IPL than in the INL (Fig 1d). One potential source for the differing SHG/fluorescence ratio may relate to the requirement for molecular asymmetry in generating the SHG signal (Moreaux et al., 2000). In the INL, it is expected that oriented membranes and less densely packed molecules and would reduce the likelihood that the distribution of dye molecules is symmetric within a small volume.

Laser scanning as visual stimulus in the retina

It is known that laser scanning can function as a visual stimulus at 930 nm in the salamander retina (Denk and Detwiler, 1999), which is dominated by long wavelength cones. Even at our chosen wavelength of 970 nm, at slow scan rates (< 10 Hz) we observed ganglion responses synchronized to the laser as previously observed (Denk and Detwiler, 1999). To test whether a 20 Hz scan rate would modulate the spiking response of ganglion cells, we measured the power of Fourier transform (FFT) of the extracellular ganglion cell response, and compared the response at 20 Hz to the response for a 1 Hz visual stimulus. At a 20 Hz scan rate, for all cells the FFT power at the laser scanning frequency was less than 1% of the FFT power at the visual stimulus frequency. However, it is possible that there are subthreshold effects that cannot be measured from spiking activity. We therefore performed intracellular recordings and tested the effect of laser scanning by itself and in combination with visual stimulus.

Figure S1 shows the response of an Off-type amacrine cell recorded intracellularly. In response to a 10 Hz scanning laser centered over the cell's receptive field, there was a measurable response of 1 – 2 mV, compared to a response of tens of mV to a 1 Hz uniform-field visual stimulus. However, the response to the laser at 20 Hz was at least 3000 fold smaller as

measured using an FFT, and was not detectable (Fig. S1b right). We then examined the response to a uniform field Gaussian flicker at low contrast (12%) with and without laser scanning at 10Hz (Fig. S1c). We computed a linear-nonlinear (LN) model consisting of a linear temporal filter representing the average response to a small flash of light and a nonlinear response function that captured any rectification or saturation of the response (Baccus & Meister, 2002). The temporal filters and nonlinearities (Fig. S1c) were nearly identical with and without the laser. We chose a 20 Hz scan rate for our standard experimental condition.

Photoelectric artifact

The laser produced a photoelectric artifact on the titanium nitride electrodes if the imaged area was located directly over the array. This problem was avoided by imaging adjacent to the array (Fig 3a). Amacrine and ganglion cell receptive fields thus partially overlapped, and therefore the imaged amacrine cells were likely exposed to greater background illumination from the laser than were ganglion cells. Although this additional background illumination would result in a slightly different state of luminance adaptation and potentially lower contrast, intracellular recordings indicated that the laser did not reduce sensitivity for the visual stimulus, even when directly centered over the receptive field center (Fig. S1c).

Visual Stimuli

Visual stimuli including uniform flashes, random checkerboards and moving bars were projected from a CRT monitor using Psychophysics Toolbox. To prevent the PMT from detecting the visual stimulus, only the red gun of the CRT was used and two long pass filters (XF3094, 610ALP, Omega Optical) inserted in the visual stimulus pathway restricted the wavelength of the visual stimulus to longer than 610 nm. The mean luminance was approximately 30 mW/m^2 and the diameter of the stimulus was ~ 1 mm on the retina. For experiments presenting a moving dark bar the background illumination was ~60 mW/m^2. Periodic stimuli were generally repeated 140 times (1Hz, 140 s) and the average response is shown. Random checkerboard stimuli were presented for 150 s. As mentioned previously, laser light (one-photon, see (Denk and Detwiler, 1999)) can stimulate photoreceptors, likewise for fluorescence and SHG signals. These effects are minimized two ways: first, by having a sufficiently high frame rate (~20Hz) so that this illumination serves as background only and does not modulate cell responses in time, and second, to use a high background luminance for the visual stimulus so that photoreceptors adapted to this background will be relatively insensitive to these other light sources.

Regions of Interest

All somas in the inner nuclear layer generated an SHG signal. The average response image across the entire recording was processed to enhance its contrast, and then thresholded to identify regions of interest with a large mean SHG signal. When the dye FM4-64 is bath applied (as opposed to picospritzing) there is an initial few seconds when the mean SHG signal decreases but thereafter it remains stable for the rest of the recording (~150 s). The time-varying signal for each pixel was then binned relative to the stimulus. These anatomically based ROIs might include pixels from more than one cell, so principal components analysis was used to identify pixels that were responding differently from the first principle component and these pixels were rejected from the ROI. ROIs were accepted as belonging to a cell if they were larger than 20 pixels, had a SNR of greater than 2, and did not span the membrane of more than one cell. This yielded ROIs with visual responses that overlaid cell membranes. Multiple ROIs that appeared to belong to the same cell were grouped together as one cell.

Signal to Noise Ratio

Although SHG is capable of very high temporal resolution (~1 ms) (Dombeck et al., 2005), we generally binned image data relative to either the stimulus or spike times by increments of 25

ms to improve the signal to noise ratio. The average correlation with both the visual stimulus and with ganglion cell spikes was comprised primarily of slower variation, consistent with electrophysiological measurements (Baccus and Meister, 2002; Olveczky et al., 2003). Some recordings, however, showed a higher SNR, demonstrating that high temporal resolution (5 ms bins) is possible with SHG imaging given sufficient SNR or signal averaging (Fig. S2a).

We also examined whether responses were stable over time during our recordings (Fig S2b). Although the amplitude of the response in terms of fractional change in SHG was stable over 140 s, noise did appear to increase slightly over time, likely due to a decrease in the absolute amplitude of the SHG response due to bleaching. Because signals were always computed as a fraction of SHG at the current time, this change over time did not influence our results.

Receptive fields

Spatial receptive fields and temporal filters were calculated by the standard method of reverse correlation with a visual stimulus consisting of binary squares (Chichilnisky, 2001), such that

$$F(x,y,\tau) = \int_0^T s(x,y,t-\tau)\, r(t)\, dt\,, \qquad (1)$$

where $F(x,y,\tau)$ is the linear response filter at position (x,y) and delay τ, $s(x,y,t)$ is the stimulus intensity at position (x,y) and time t, normalized to zero mean, $r(t)$ is the firing rate of a cell, and T is the duration of the recording. The filter $F(x,y,\tau)$ was computed by correlating the visual stimulus to spike times for ganglion cells. A temporal filter was computed as the spatial average of *F*(). The stimulus $s(x,y,t)$ was convolved with the filter $F(x,y,\tau)$ to obtain the linear prediction of the response. A static non-linearity was computed as the average relationship between the firing rate of the cell and the linear prediction.

Modelling of motion anticipation by amacrine cells, three models:
The LN model

The above mentioned receptive field filter and non-linearity were computed for each Off ganglion cell (n=115). A moving bar stimulus was convolved with the receptive field filter to obtain a linear prediction *L(t)*,

, (2)

where is the moving bar stimulus and is the space-time receptive field filter computed from a white noise stimulus, and averaged over the spatial dimension of the extent of the bar. The LN model consisted of the linear prediction and non-linearity getting rescaled so that when the linear prediction is passed through the non-linearity the peak firing rate of the LN model matched the actual peak firing rate. This rescaling represents the fact that maximal firing rate to a moving bar stimulus is generally much greater than to a white noise checkerboard stimulus,

, (3)

where is the rescaled non-linearity computed from the white-noise stimulus and is the firing rate of the LN model.

The SLN model: subtractive inhibition and disinhibition

The filter of the LN model described above includes amacrine cell responses to a white noise checkerboard stimulus and thus it includes the linear component of the amacrine cell

contribution to the ganglion cell receptive field. We wished to determine the possible nonlinear contribution that amacrine cells might have to change the response of the cell a moving bar stimulus. The general structure of this model was to optimize a weighted combination of amacrine cell type responses, which was used to modify the linear component of the LN model and passed through the same non-linearity as the LN model to yield a firing rate that matches the data by minimizing rms error. Models were fit to one half of the data and tested on the other half. All reported results are from this held out data.

Amacrine cell responses to the moving bar stimulus (n = 365) were clustered (by k-means) into three general categories as shown in Fig. 3e, (Off, Biphasic, and On) and then further divided the Biphasic class into Fast and Slow classes. We verified by F-test that the four parameter model (Off, fast Biphasic, slow Biphasic and On) was significantly better (p = 3.5e-11) than the three parameter model (Off, Biphasic, On) on held out data. Subdividing Off and On cell classes did not improve the model.

To account for transmission delays and spatial weighting connections between amacrine and ganglion cells, we used a temporal and spatial filter taken from (Manu and Baccus, 2011), which injected current into sustained Off amacrine cells and measured the temporal filter and spatial spread of inhibition on nearby Off ganglion cells

$$A_i(t) = \sum_j e^{-\frac{d}{\lambda}} A_j(t + t_0), \tag{4}$$

where $A_j(t-t_0)$ is an individual amacrine cell response to the moving bar whose response has been delayed by t_0 (25 ms), which represents the delay of the amacrine cell transmission filter (Manu and Baccus, 2011), d is the distance between amacrine cell j and a ganglion cell, λ (83 μm) is the space constant that describes the amacrine cell influence as a function of distance for a particular type of amacrine cell, (Manu and Baccus, 2011) and A_i is the spatially weighted summed responses for one of the four types of amacrine cells i. The amacrine input A_i is computed separately for each ganglion cell because every ganglion cell will have different spatial weightings from the same amacrine cells. The spatially weighted summed amacrine responses A_i were then optimally weighted (to minimize rms error between the model and data) by ω_i (allowed to be negative or positive) and summed to produce I:

(5)

. A single value of ω_i was applied to each of the four amacrine cell types, so this spatial weighting consisted of four parameters. The total subtractive amacrine input was subtracted from the linear prediction L from the LN model and passed through the same non-linearity to obtain the firing rate for this version of the model,

, (6)

The DLN model: divisive gain control

Alternatively, the linear prediction could be modified by dividing by amacrine responses. In practice it is not desirable to divide by zero, or a negative number, or a very small number, so the following formulation was used:

(7)

. (8)

The constant *c* was used to avoid dividing by a small number, and is a global free parameter (fit to minimize population rms error). Both subtractive and divisive models were formulated so that when all the weights ω_i are zero these models are equivalent to the LN model. Also, the A_i terms are normalized in rms amplitude so that the weights ω_i can be interpreted as the relative contribution of a particular type of amacrine cell.

It is important to point out the known limitations and simplifications of this model given what we know about the retina. Ideally there would be different space constants λ for each of the four types of amacrine cells, but this is unknown, and a limitation of the model. However, because nearby effects are considered and the moving bar is spatially localized in the direction of motion, it is expected that long-distance connections do not play a role except in the direction of the extent of the bar, where these effects would become summed effects within the model. Likewise, transmission filters may vary between different pairs of amacrine and ganglion cells. Finally what we are defining as a class of of amacrine cells is defined solely by response to a moving bar, and likely contains multiple types of amacrine cells.

Fitting the models

Because the fit of the model consisted only of four (SLN) or five (DLN) free parameters, models were fit by a grid search by calculating the total error for every value of weight in the stimulus space (-1.0 to +1.0) and choosing the solution with the lowest total error. The total error consists of the RMS error between the data and either the divisive or subtractive model plus a quadratic penalty (α) on the sum of the weights:

$$Total\ error = \sqrt{\frac{1}{n}\sum_{t=0}^{n}(FR[model] - FR[data])_t^2} + \alpha\sum_{i=1}^{4}\omega_i^2 \qquad (9)$$

The value of α was determined by a 10% increase in RMS error compared to the RMS error when α = 0. This penalty on the weights reduces overfitting and drives the solution towards smaller values of weights which is relatively closer to the simplest model: the LN model. The value of α for the divisive model was 0.71 and the value for the subtractive model was 0.824.

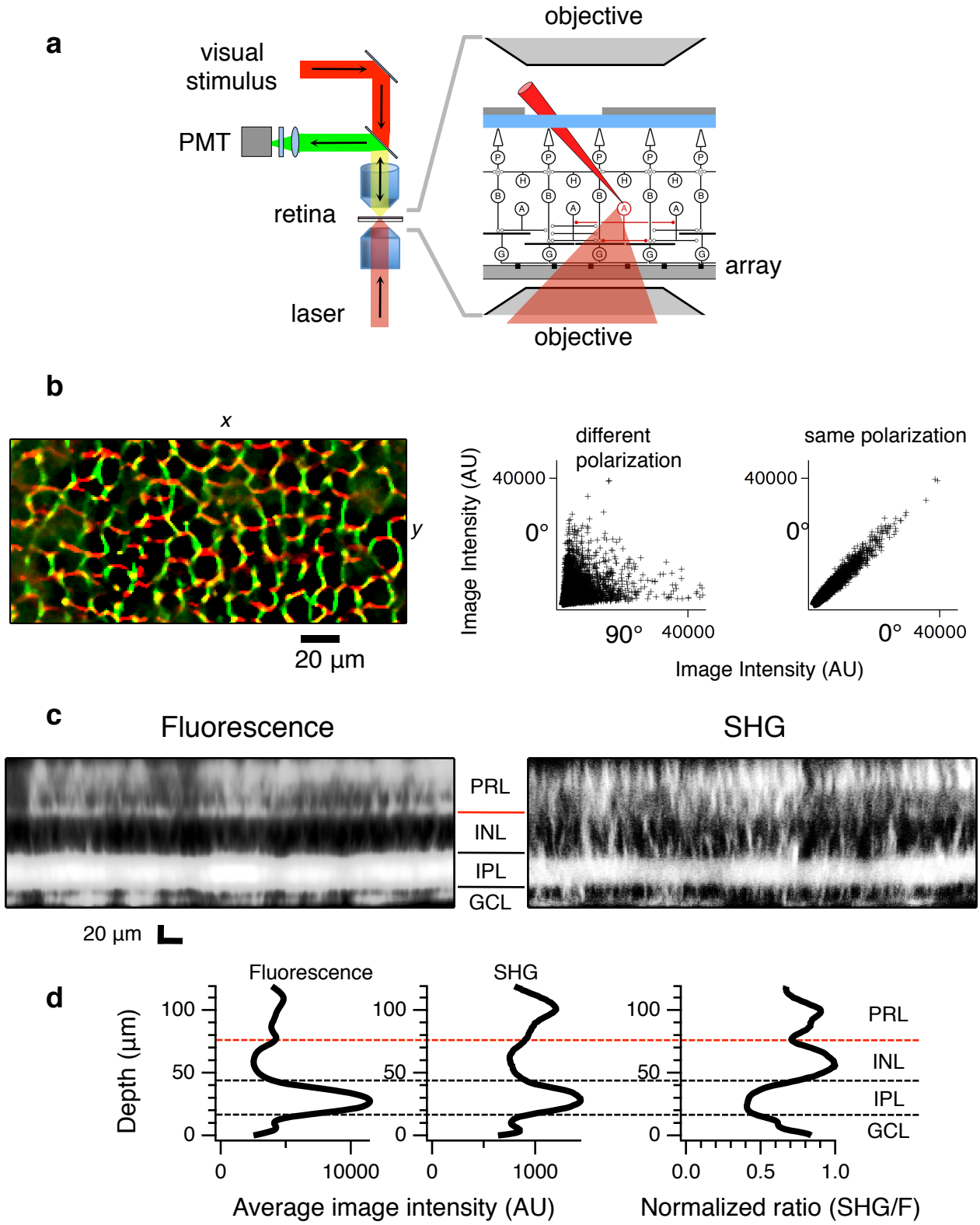
a
visual stimulus
PMT
retina
laser
objective
array
objective
b
x
y
20 µm
different polarization
same polarization
Image Intensity (AU)
40000
0°
90°
40000
0°
40000
0°
40000
Image Intensity (AU)
c
Fluorescence
SHG
PRL
INL
IPL
GCL
20 µm
d
Fluorescence
SHG
Depth (µm)
100
50
0
0
10000
0
1000
0.0
0.5
1.0
PRL
INL
IPL
GCL
Average image intensity (AU)
Normalized ratio (SHG/F)

Figure 1

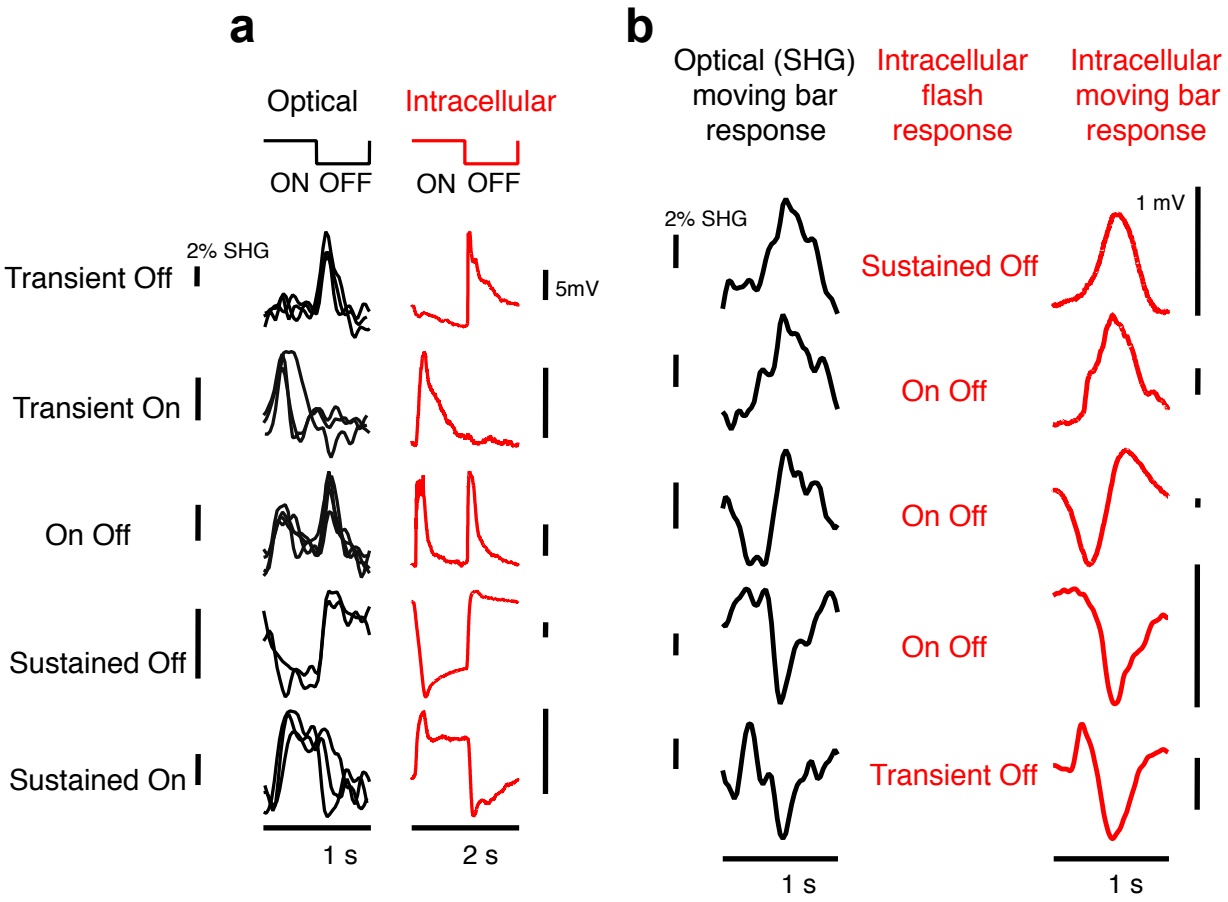
a
Optical
Intracellular
ON OFF
ON OFF
2% SHG
5mV
Transient Off
Transient On
On Off
Sustained Off
Sustained On
1 s
2 s
b
Optical (SHG) moving bar response
Intracellular flash response
Intracellular moving bar response
2% SHG
1 mV
Sustained Off
On Off
On Off
On Off
Transient Off
1 s
1 s

Figure 2

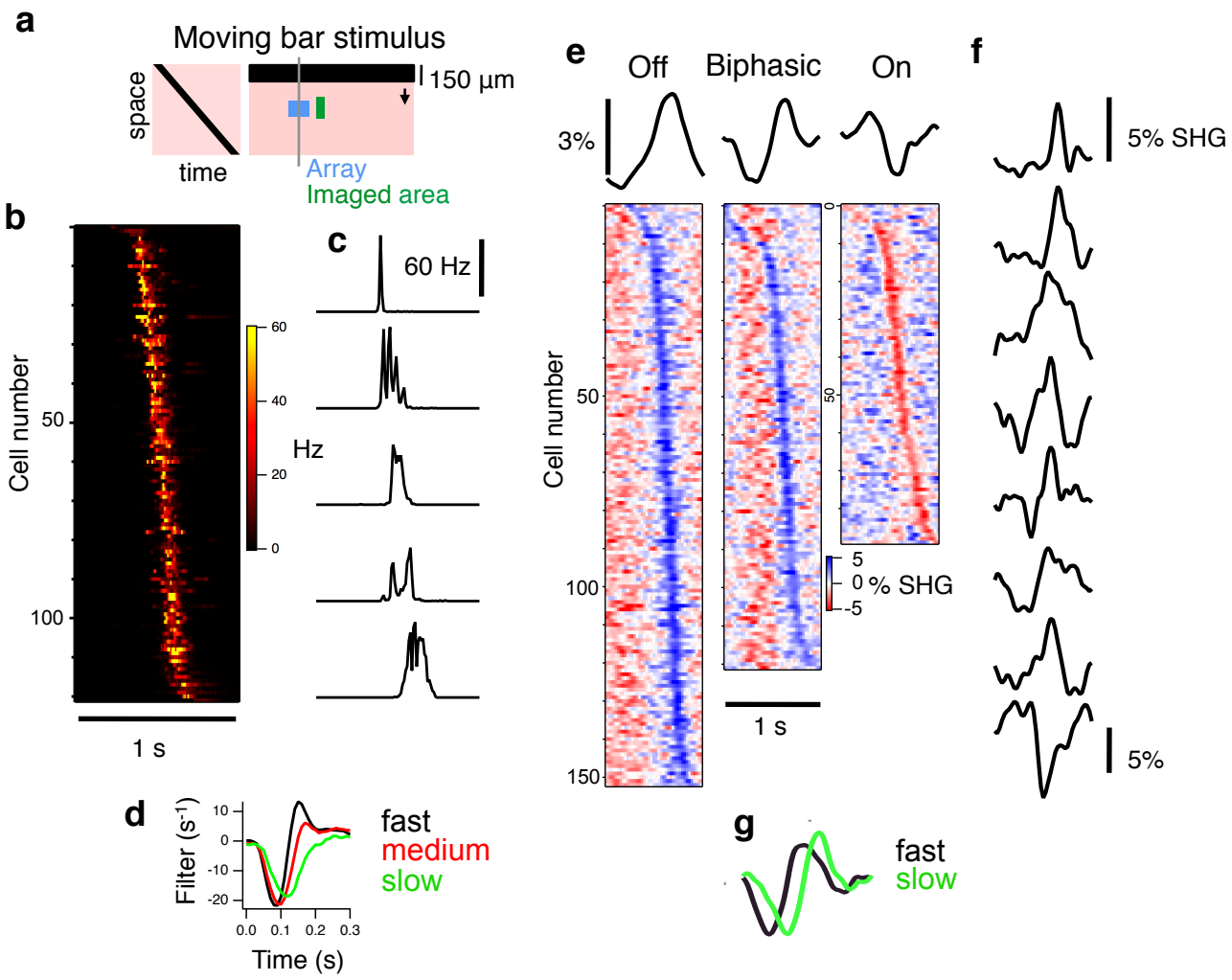
a
Moving bar stimulus
space
time
150 µm
Array
Imaged area
b
Cell number
50
100
1 s
60
40
20
0
Hz
c
60 Hz
d
Filter (s-1)
10
0
-10
-20
0.0
0.1
0.2
0.3
Time (s)
fast
medium
slow
e
Off
Biphasic
On
3%
Cell number
50
100
150
1 s
5
0
-5
% SHG
f
5% SHG
5%
g
fast
slow

Figure 3

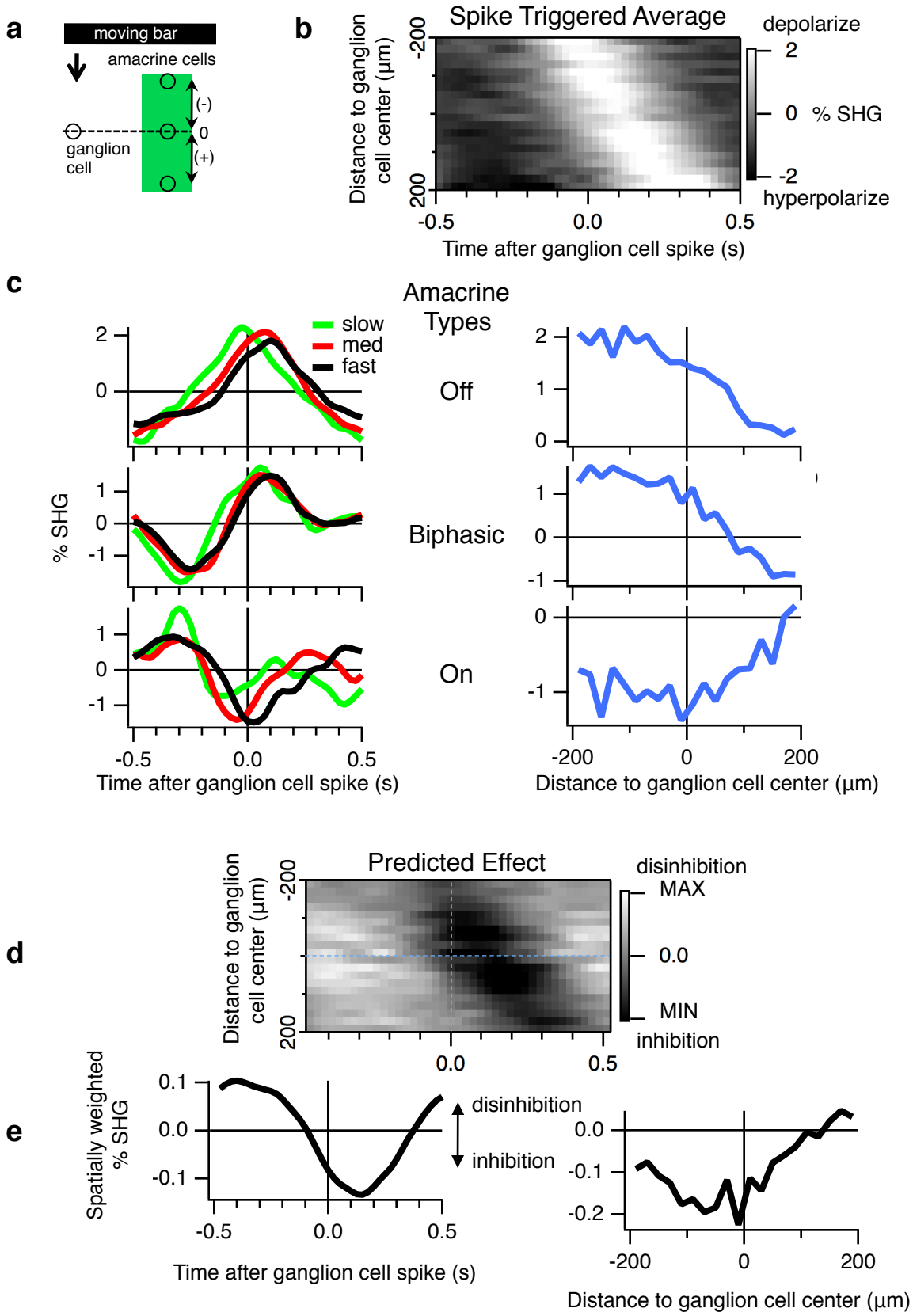
a
moving bar
amacrine cells
(-)
0
(+)
ganglion cell
b
Spike Triggered Average
Distance to ganglion cell center (µm)
-200
200
-0.5
0.0
0.5
Time after ganglion cell spike (s)
depolarize
2
0
% SHG
-2
hyperpolarize
c
Amacrine Types
slow
med
fast
Off
Biphasic
On
% SHG
Time after ganglion cell spike (s)
Distance to ganglion cell center (µm)
d
Predicted Effect
Distance to ganglion cell center (µm)
disinhibition
MAX
0.0
MIN
inhibition
e
Spatially weighted % SHG
disinhibition
inhibition
Time after ganglion cell spike (s)
Distance to ganglion cell center (µm)

Figure 4

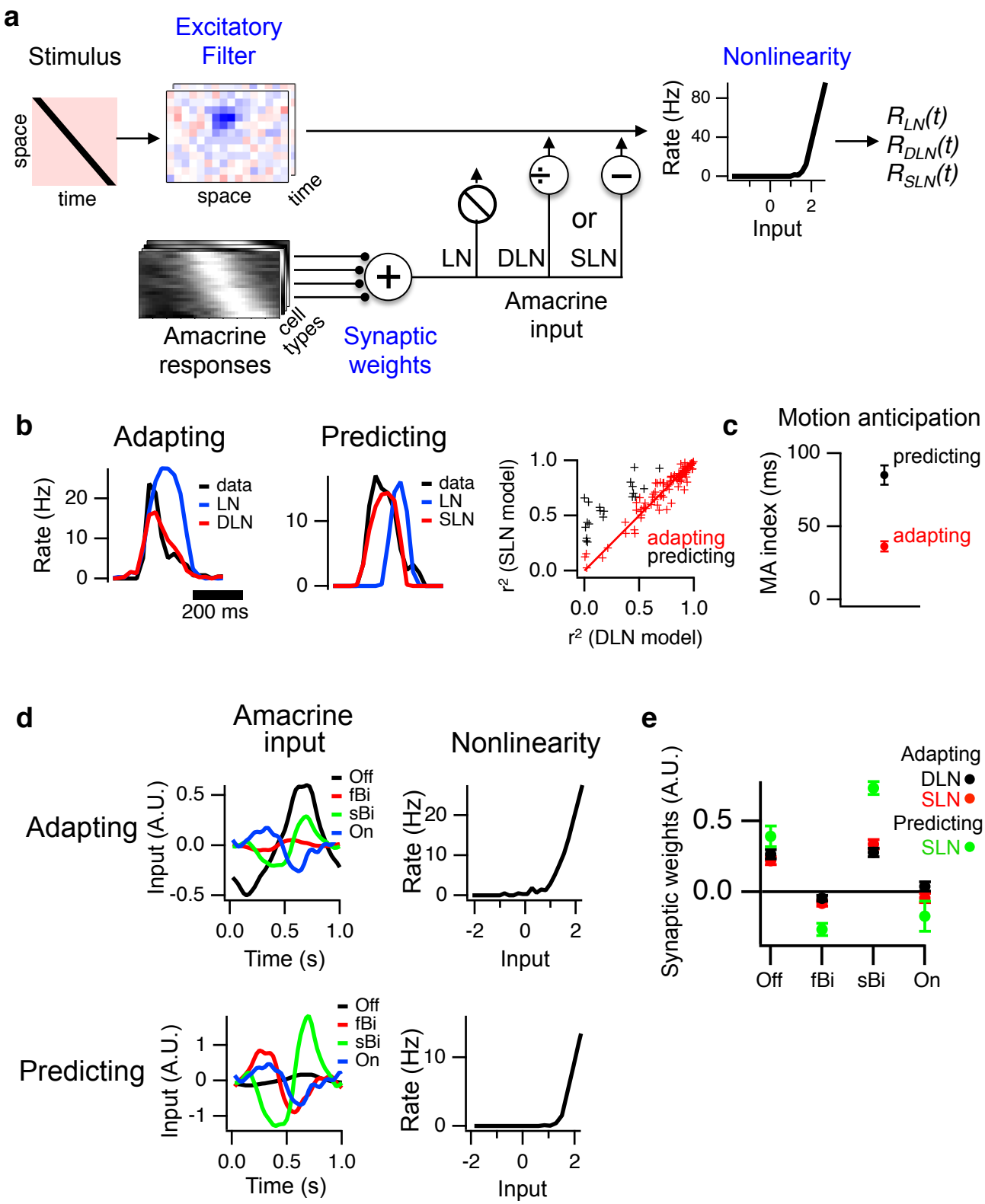
a
Stimulus
Excitatory Filter
Nonlinearity
space
time
space
time
Rate (Hz)
80
40
0
0
2
Input
$R_{LN}(t)$
$R_{DLN}(t)$
$R_{SLN}(t)$
LN
DLN
or
SLN
Amacrine input
Amacrine responses
cell types
Synaptic weights
b
Adapting
Predicting
Rate (Hz)
20
10
0
data
LN
DLN
200 ms
10
0
data
LN
SLN
1.0
0.5
0.0
r^2 (SLN model)
adapting
predicting
0.0
0.5
1.0
r^2 (DLN model)
c
Motion anticipation
MA index (ms)
100
50
0
predicting
adapting
d
Amacrine input
Nonlinearity
Adapting
Input (A.U.)
0.5
0.0
-0.5
Off
fBi
sBi
On
0.0
0.5
1.0
Time (s)
Rate (Hz)
20
10
0
-2
0
2
Input
Predicting
Input (A.U.)
1
0
-1
Off
fBi
sBi
On
0.0
0.5
1.0
Time (s)
Rate (Hz)
10
0
-2
0
2
Input
e
Synaptic weights (A.U.)
0.5
0.0
Adapting
DLN
SLN
Predicting
SLN
Off
fBi
sBi
On

Figure 5

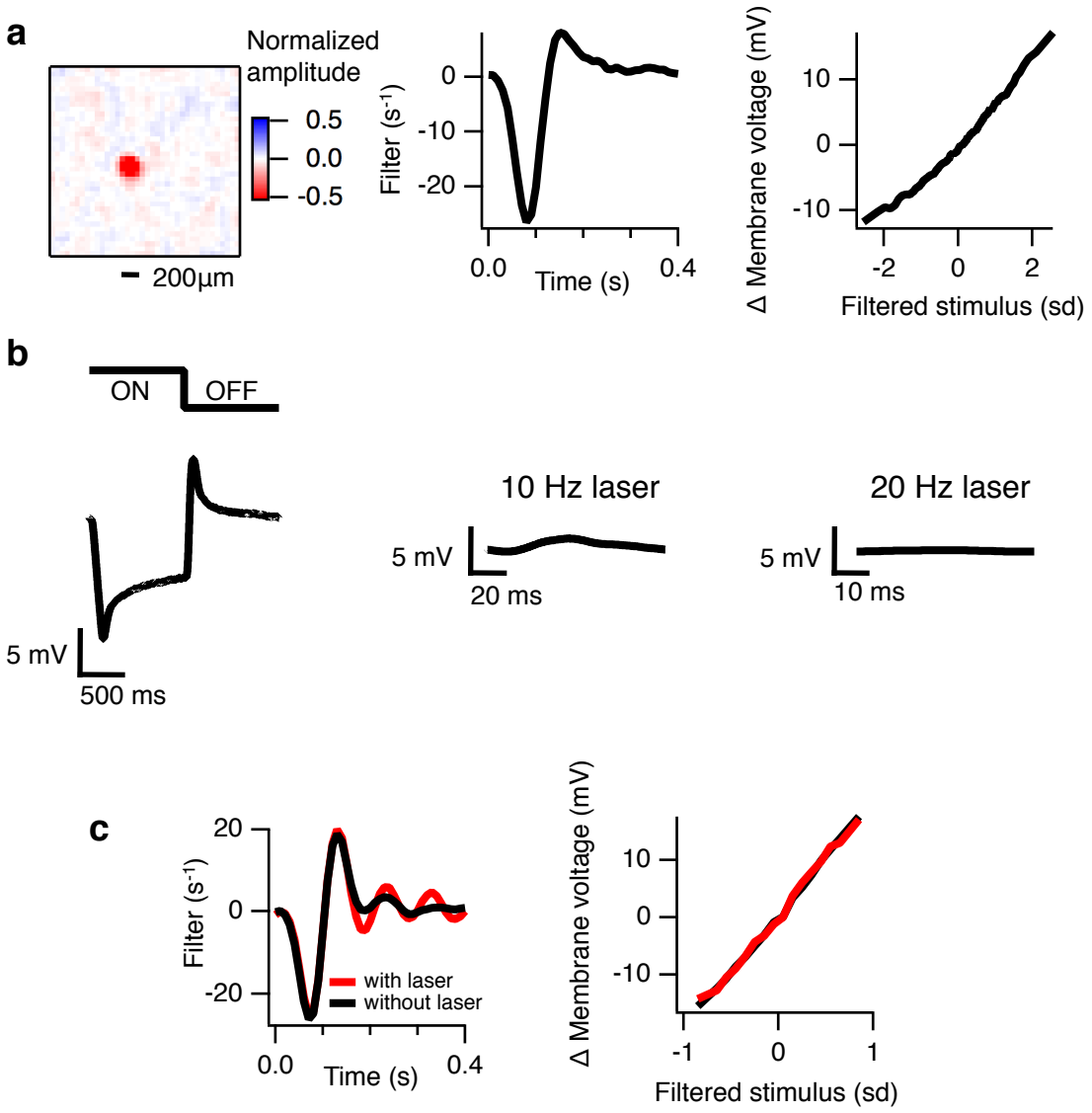
a
Normalized amplitude
0.5
0.0
-0.5
200µm
Filter (s-1)
0
-10
-20
0.0
Time (s)
0.4
Δ Membrane voltage (mV)
10
0
-10
-2
0
2
Filtered stimulus (sd)
b
ON
OFF
5 mV
500 ms
10 Hz laser
5 mV
20 ms
20 Hz laser
5 mV
10 ms
c
Filter (s-1)
20
0
-20
with laser
without laser
0.0
Time (s)
0.4
Δ Membrane voltage (mV)
10
0
-10
-1
0
1
Filtered stimulus (sd)

Figure S1

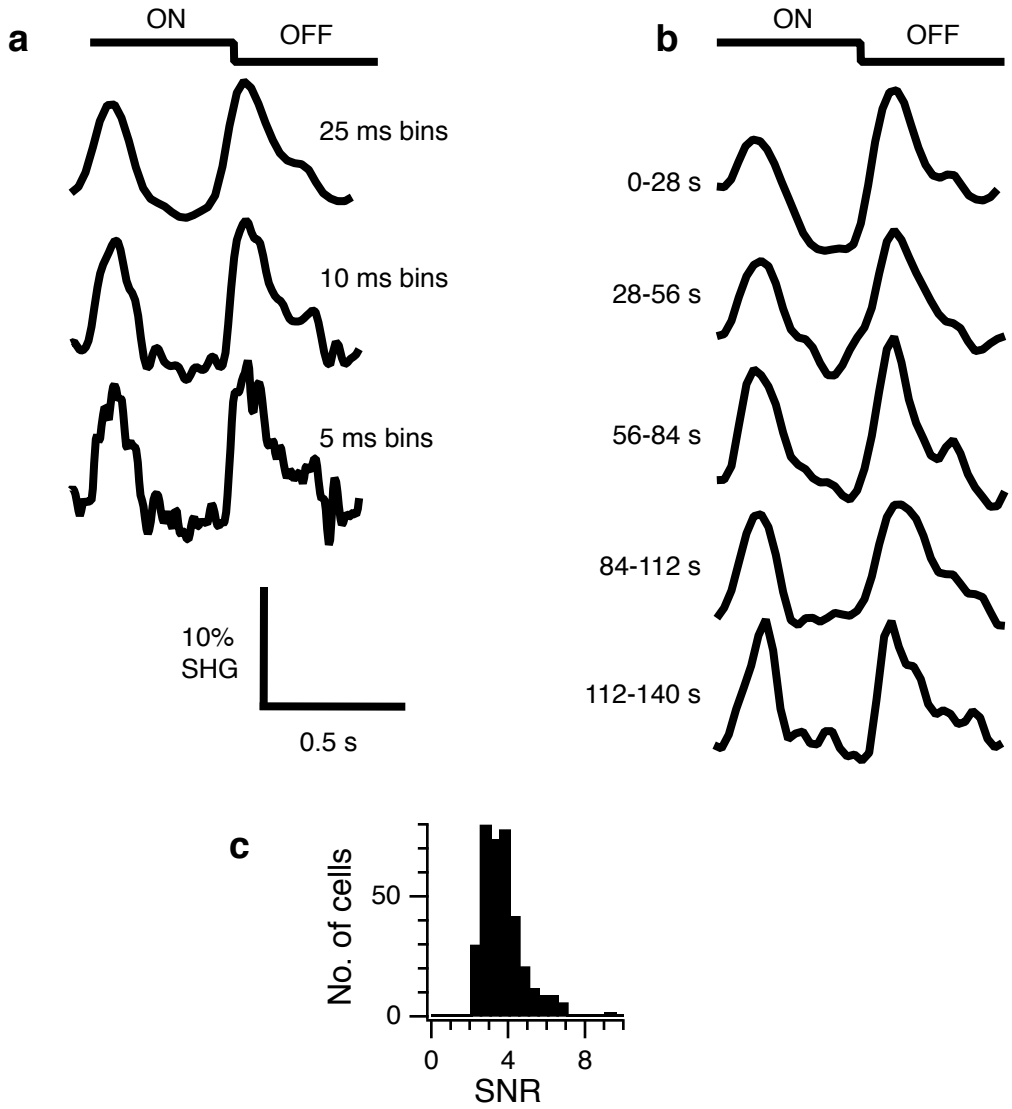
a
ON
OFF
25 ms bins
10 ms bins
5 ms bins
10%
SHG
0.5 s
b
ON
OFF
0-28 s
28-56 s
56-84 s
84-112 s
112-140 s
c
No. of cells
50
0
0
4
8
SNR

Figure S2

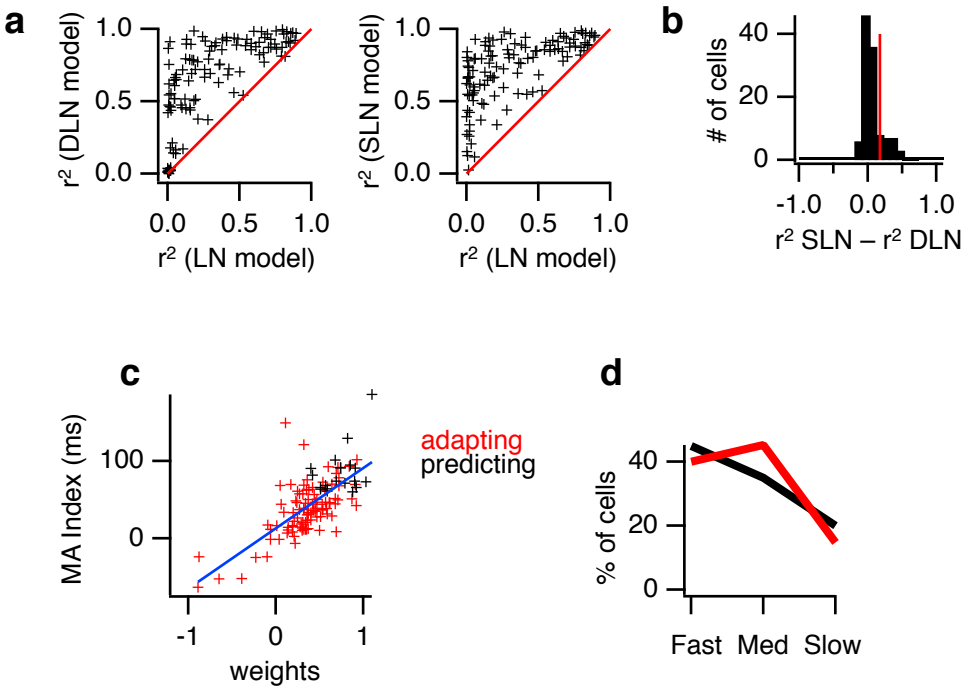
a
1.0
0.5
0.0
r2 (DLN model)
0.0
0.5
1.0
r2 (LN model)
1.0
0.5
0.0
r2 (SLN model)
0.0
0.5
1.0
r2 (LN model)
b
40
20
0
# of cells
-1.0
0.0
1.0
r2 SLN – r2 DLN
c
100
0
MA Index (ms)
-1
0
1
weights
adapting
predicting
d
40
20
0
% of cells
Fast
Med
Slow

Figure S3